

# A New Insight into Non-covalent Interactions in 1,4-Disubstituted 1H-1,2,3-Triazole: Synthesis, X-ray structure, DFT calculations, *in vitro* Lipoxygenase Inhibition (LOX) and *in silico* Studies

Muhammad Naeem Ahmed<sup>a,\*</sup>, Sadia Shabbir<sup>a</sup>, Bakhtawar Batool<sup>a</sup>, Tariq Mahmood<sup>b</sup>, Umer Rashid<sup>b</sup>, Khawaja Ansar Yasin<sup>a</sup>, Muhammad Nawaz Tahir<sup>c</sup>, M. L. Arias Cassar<sup>d</sup>, Diego M. Gil<sup>e,#,\*</sup>

<sup>a</sup> Department of Chemistry University, The University of Azad Jammu and Kashmir, Muzaffarabad 13100, Pakistan.

<sup>b</sup> Department of Chemistry, COMSATS University Islamabad, Abbottabad Campus, University Road, Tobi Camp, Abbottabad-22060, Pakistan

<sup>c</sup> Department of Physics, University of Sargodha, Sargodha, Pakistan

<sup>d</sup> Cátedra de Química Orgánica I. Instituto de Química Orgánica. Facultad de Bioquímica, Química y Farmacia. Universidad Nacional de Tucumán. Ayacucho 471. T4000INI. San Miguel de Tucumán. Argentina.

<sup>e</sup> INBIOFAL (CONICET – UNT). Instituto de Química Orgánica. Facultad de Bioquímica, Química y Farmacia. Universidad Nacional de Tucumán. Ayacucho 471. T4000INI. San Miguel de Tucumán. Argentina

## ARTICLE INFO

### Article history:

Received 22 December 2020

Revised 25 February 2021

Accepted 8 March 2021

Available online 15 March 2021

### Keywords:

Triazole

DFT

Non-covalent interactions

LOX

Docking

## ABSTRACT

Present work deals with the synthesis, characterization, structural properties and *in silico* studies of ethyl 6-(4-(cyclohexylmethyl)-1H-1,2,3-triazol-1-yl)pyridine-3-carboxylate (1). The synthesized derivative was characterized by spectroscopic as well as single crystal XRD technique. The structure reveals weak non-covalent contacts such as C-H... $\pi$ , lone pair... $\pi$  and  $\pi$ ... $\pi$  stacking interactions along with C-H...O and C-H...N hydrogen bonds to form the supramolecular assembly. A detailed analysis of the intermolecular interactions was performed by using the Hirshfeld surface analysis and energy framework calculations, indicating that the dispersion energy is dominant over the electrostatic one in all the structural dimer studied. In addition, the intermolecular interactions have been characterized using the quantum theory of "atoms in molecules", molecular electrostatic potential (MEP) and the non-covalent interaction plot (NCI plot) index analysis. Compound displayed the IC<sub>50</sub> value of IC<sub>50</sub> = 37.40  $\mu$ M in comparison to reference drug indomethacin (IC<sub>50</sub> = 48.25  $\mu$ M) against lipoxygenase (LOX). Docking studies revealed important interactions and binding energy of the compound in comparison with the standard drugs used.

© 2021 Elsevier B.V. All rights reserved.

## 1. Introduction

Triazole derivatives are of great importance in medicinal chemistry because they can be used for the preparation of a great variety of heterocyclic compounds with different biological activities including anticancer [1], antitumor [2], antimalarial [3], antitubercular [4], antileishmanial [5], antifungal [6], antibacterial [7], antihypertensive [8], among other activities. The importance of triazole derivatives in medicinal chemistry is mainly related with some structural properties such as high dipole moment, rigidity, and capability to bind with a great variety of enzymes and receptors through weak intermolecular interactions (hydrogen bonds,

dipole-dipole and  $\pi$ -stacking) when they bind with the biological target [9]. There are many derivatives of 1-(pyridine-2-yl)-1,2,3-triazole and tetrazolo[1,5-a]pyridines that act as an intermediate in organic synthesis or as ligands in coordination compounds and have shown biologically important properties [10].

Animal tissues respond to harsh external factors like pathogens, irritants by higher migration of certain neutrophils and macrophages to the affected site. Increased blood flow, elevated cellular metabolism, vasodilatation may be amongst many of the initial symptoms. Lipoxygenase can be regarded as important factor in enhancing the inflammatory reactions. Lipoxygenase enzymes play a key role in converting arachidonic acid to biologically active leukotrienes, which in turn are responsible for many inflammatory and allergic reactions [11]. These leukotrienes are notorious for the allergic indications caused by their inflammatory reactions. The inflammatory phase may be treated by inhibition of 15-lipoxygenase pathway [12]. LOXs are sensitive to antioxidants

\* Corresponding authors.

E-mail addresses: [drnaem@ajku.edu.pk](mailto:drnaem@ajku.edu.pk) (M.N. Ahmed), [diego.gil@fbqf.unt.edu.ar](mailto:diego.gil@fbqf.unt.edu.ar) (D.M. Gil).

# Member of the Research Career of CONICET.

as they are involved in inhibition of lipid hydroperoxide formation due to scavenging of lipid oxy- or peroxyradicals and can minimize LOX catalysis by less availability of lipid hydroperoxide substrate [13]. Studies have shown that blockade of arachidonic acid metabolism through inhibition of lipoxygenase activity will ultimately be helpful in reducing the inflammatory effects. Scaffolds used for scavenging alkyl/ aryl oxygen free radicals have been used as anti-inflammatory agents. Different isomeric triazole derivatives [14] are also known for their oxygen free radicals scavenging properties.

Non-covalent interactions play a relevant role in a variety of molecular architectures, supramolecular assembly and crystal engineering. In addition, some conventional X-H...X and unconventional C-H...Y (being X or Y = F, Cl, O, N or S) hydrogen bonds, C-H... $\pi$ , lone pair... $\pi$  and  $\pi$ ... $\pi$  stacking interactions are the most important and widely studied to understand the supramolecular architectures of organic and inorganic compounds [15a]. In continuation of our work of search for the newer models having undisputable structures [15b-d] for the known ailments through azole chemistry [16], we have designed and synthesized new derivatives of 1,2,3-triazole bearing substituent at position 1 and 4 of the triazolo ring [16b,17]. The synthesized compound was characterized by  $^1\text{H}$  and  $^{13}\text{C}$  Nuclear Magnetic Resonance (NMR), UV-Vis and IR spectroscopy. The crystal structure of the title compound was solved by X-ray diffraction methods a detailed analysis of the intermolecular interactions has been performed by using the Hirshfeld surface analysis and DFT calculations. In addition, the lipoxygenase (LOX) activity of 1,4-disubstituted 1,2,3-triazole was determined by a spectrophotometric method and the binding affinity values of the native ligand, the title compound and the reference drug were obtained by Docking studies.

## 2. Experimental

### 2.1. Synthesis.

Target compound was synthesized by already reported procedure with slight modification [10,16b]. A solution containing 1 mmol of ethyl tetrazolo[1,5-a]pyridine-6-carboxylate and 0.1 mmole of  $\text{Cu}(\text{OAc})_2$  in THF was stirred at room temperature. Then (prop-2-ynyl)cyclohexane (1.1 mmole) was added and the reaction mixture was stirred at room temperature for 20 min under THF (Scheme 1). The progress of reaction was monitored through thin layer chromatography (TLC) and the remaining solvent was removed under vacuum. The residue was purified by flash column chromatography (FCC) to give target molecule.

**Ethyl 6-(4-(cyclohexylmethyl)-1H-1,2,3-triazol-1-yl)pyridine-3-carboxylate (1).** White crystalline solid, m.p. = 124–125°C,  $R_f$  = 0.45 (n-hexane: EtOAc), IR (KBr,  $\text{cm}^{-1}$ ):  $\nu$  3140, 3060, 2845, 1710, 1591. 1485  $^1\text{H}$ NMR ( $\text{CDCl}_3$ )  $\delta$  9.02 (d, 1H, H-C(8)), 8.45 (dd, 1H, H-C(5)), 8.32 (s, 1H, H-C(9)), 8.24 (d, 1H, H-C(6)), 4.45 (q, 2H, H-C(2)), 2.70 (d, 2H, H-C(11)), 1.75–1.62 (m, 5H, H-C(13), H-C(14), H-C(15), H-C(16), H-C(17)), 1.42 (t, 3H, H-C(1)), 1.34–0.90 (m, 6H, H-C(12), H-C(13), H-C(14), H-C(15), H-C(16), H-C(17));  $^{13}\text{C}$  NMR ( $\text{CDCl}_3$ )  $\delta$  166.0 (C(3)), 152.6 (C(8)), 150.2 (C(10)), 146.7 (C(7)), 140.1 (C(5)), 125.5 (C(4)), 117.8 (C(6)), 112.9 (C(9)), 60.6 (C(2)), 38.8 (C(12)), 33.3 (C(11)), 32.5 (C(13)–(17)), 26.2 (C(15)), 26.0 (C(16)–(14)), 14.0 (C(1)), Elemental analysis calculated for  $\text{C}_{17}\text{H}_{22}\text{N}_4\text{O}_2$  (314.174): C, 64.95; H, 7.05; N, 17.82. Observed: C, 64.90; H, 7.11; N, 17.75.

### 2.2. Instrumentation.

Melting points were determined on a Yanaco melting point apparatus and are uncorrected. IR spectrum was recorded on a Nicolet FTIR 5DX spectrometer using KBr disc method.  $^1\text{H}$ -NMR and

$^{13}\text{C}$ -NMR spectra were recorded on a JEOL JNM-ECA 300 MHz spectrometer. Tetramethylsilane (TMS) was used as reference.

### 2.3. Crystal data and structure refinement.

Suitable single crystals of compound **1** were selected for X-ray analyses and diffraction data were collected on a Bruker Kappa APEX-II CCD detector with  $\text{MoK}\alpha$  radiation at 100 K. Using the SADABS program semi empirical correction was applied [18a]. SHELX program was also used to solve all structures by direct method [18b]. Positions and anisotropic parameters of all non-H atoms were refined on  $F^2$  using the full matrix least-squares technique. The H atoms were added at geometrically calculated positions and refined using the riding model [18c]. The details of crystallographic data and crystal refinement parameters for the compound **1** is given in Table 1.

### 2.4. Hirshfeld surface calculations.

An analysis of the Hirshfeld surfaces and the corresponding 2D fingerprint plots (full and decomposed) [19] was carried out employing *CrystalExplorer*17.5 [20] program to visualize and quantify different molecular interactions. The Hirshfeld surfaces were mapped over  $d_{\text{norm}}$  and *shape index* properties. The  $d_{\text{norm}}$  is a symmetric function of distances to the surface from nuclei inside and outside the HS (*di* and *de*, respectively), relative to their respective van der Waals (vdW) radii, which enables identification of the regions of particular importance to intermolecular interactions. The  $d_{\text{norm}}$  surfaces were mapped over a fixed color scale of  $-0.050$  au (red) –  $0.750$  Å au (blue). The *shape-index* property is based on the local curvature of the surface, and it is especially useful to identify planar  $\pi$ -stacking arrangements [19a].

### 2.5. Theoretical methods

All quantum chemical calculations were carried out by using the Gaussian 09, Rev D.01 software package [21]. The molecular structure of the title compound was optimized using the experimental single-crystal X-ray data at the B3LYP/6-311G(d,p) level of theory [22]. Frequency calculations on optimized geometry indicate that all stationary points were found to be true minima (zero imaginary frequencies) on the potential energy surface. Time-dependent density functional theory (TD-DFT) approach was used to calculate the absorption properties at the same level of theory and taking into account the solvent effect (ethanol) by using the conductor-like polarizable continuum model (CPCM).

The calculations of non-covalent interactions were performed using Gaussian 09, Rev D.01 [22] at the B3LYP-D3/def2-TZVP approximation. The computed interaction energies were corrected for basis set superposition errors by means of the counterpoise method (BSSE) [23]. The Grimme's D3 dispersion correction has been used in the calculations [24]. The interaction energies were computed by calculating the difference between the energies of the monomers and the ones of their assembly. The molecular electrostatic potential (MEP) surface has been computed at B3LYP-D3/def2-TZVP level of theory and the 0.001 a.u. isosurface as an estimate of the van der Waals surface. The topological analysis of electron density distribution has been analyzed with the help of quantum theory of "atoms in molecules" (QTAIM) method [25] by using the AIM2000 program [26] as well as the non-covalent interaction plot (NCI plot) [27].

### 2.6. In-vitro Lipoxygenase activity.

The lipoxygenase activity of synthesized 1,2,3-triazole was determined by spectrophotometric method with slight modification

**Table 1**  
Crystallographic data for ethyl 6-(4-(cyclohexylmethyl)-1H-1,2,3-triazol-1-yl)pyridine-3-carboxylate (1).

CCDC deposition number	1895558
<b>Crystal data</b>	
Chemical formula	C <sub>17</sub> H <sub>22</sub> N <sub>4</sub> O <sub>2</sub>
Formula weight	314.38
Crystal system, space group	Triclinic, Pī
Temperature (K)	296
Unit cell dimensions	a = 6.1192(16) Å b = 9.143(3) Å c = 15.484(5) Å α = 84.571(8)° β = 83.661(11)° γ = 79.508(8)°
Volume (Å <sup>3</sup> )	844.2(4)
Z	2
Radiation type	Mo Kα
μ (mm <sup>-1</sup> )	0.08
Crystal size (mm)	0.44 × 0.20 × 0.17
<b>Data collection</b>	
Diffractometer	Bruker Kappa APEXII CCD
Absorption correction	Multi-scan (SADABS; Bruker, 2005)
T <sub>min</sub> , T <sub>max</sub>	0.940, 0.975
N <sup>o</sup> of measured, independent and observed [I > 2σ(I)] reflections	10697, 3276, 1497
R <sub>int</sub>	0.043
(sin θ/λ) <sub>max</sub> (Å <sup>-1</sup> )	0.617
<b>Refinement</b>	
R[F <sup>2</sup> > 2σ(F <sup>2</sup> )], wR(F <sup>2</sup> ), S	0.068, 0.214, 1.03
N <sup>o</sup> of reflections	3276
N <sup>o</sup> of parameters	211
N <sup>o</sup> of restraints	2
H-atom treatment	H-atom parameters constrained
Δ <sub>max</sub> , Δ <sub>min</sub> (e Å <sup>-3</sup> )	0.23, -0.17

[28]. Inhibition was determined by measuring the loss of soybean 15-LOX activity (5 μg) with 0.2 μM linoleic acid as the substrate prepared in borate buffer (0.2 M, pH 9.0). The inhibition in triplicate at various concentrations of synthetic compound was recorded at 234 nm using UV-Vis spectrophotometer. Indomethacin was used as positive control, while methanol was used as negative control. IC<sub>50</sub> indicating the concentration of 50% inhibition was also calculated [29].

### 2.7. Molecular Docking studies.

Docking studies were carried out using Molecular Operating Environment (MOE2016.08) software. Three-dimensional crystal structure of lipoxygenase was retrieved from Protein Data Bank (PDB accession code 1JNQ). The docking algorithm was validated before docking of compound by re-dock method. The native ligand was re-docked into the binding site of the 1JNQ. The root mean square deviation (RMSD) between the re-dock and experimental pose was found within the threshold limit of < 2.0 Å (0.97 Å). The preparation of ligand and enzyme was performed according to our previously reported procedures [30],[31]. The view of the docking results and analysis of their surface with graphical representations were done using MOE and discovery studio visualizer [32].

## 3. Results and discussion

### 3.1. Chemical synthesis and characterization

The target compound ethyl 6-(4-(cyclohexylmethyl)-1H-1,2,3-triazol-1-yl)pyridine-3-carboxylate (1) was synthesized through a synthetic protocol shown in Scheme 1. The ethyl tetrazolo[1,5-a]pyridine-6-carboxylate reacted with copper acetate and (prop-2-ynyl)cyclohexane in THF as solvent. The resulting solution was stirred at room temperature during 20 minutes. The expected molecular structure has been confirmed by spectroscopic techniques and single-crystal X-ray analysis.

In the <sup>1</sup>H NMR spectra, the methylene protons belonging to the cyclohexane backbone were observed in the range 0.90–1.75 ppm as a multiplet, while the peak appeared at 2.70 ppm was assigned to the bridging methylene protons (H-C11). In addition, the protons corresponding to the pyridine ring were observed in the range of 8.24–9.02 ppm, and the chemical shift observed at 4.45 ppm as a quadruplet was assigned to the methylene ester protons. In the <sup>13</sup>C NMR spectra, the carbon peaks belonging to the pyridine ring were observed at 117.8–152.6 ppm range. The signal observed at 166.0 ppm was assigned to the ester C=O group. The methylene carbon peaks belonging to the cyclohexane backbone were observed in the range 26.0–38.8 ppm while the bridging methylene carbon was observed at 33.3 ppm. The <sup>13</sup>C NMR spectrum also exhibits characteristic signals for C9 and C10 of the triazole ring at 112.8 and 150.3 ppm, respectively. The <sup>1</sup>H and <sup>13</sup>C NMR signals with the corresponding assignments are listed in Table S1 (Supplementary material).

### 3.2. Description of crystal structure of (1).

The title compound crystallizes in the triclinic space group Pī accommodating 2 molecules per unit cell. Fig. 1 shows an ORTEP view of the molecular structure of 1 along with the optimized structure at B3LYP/6-311G(d,p) level of theory. Relevant interatomic distances, angles and torsional angles determined experimentally are listed in Table 2. In ethyl 6-[4-(cyclohexylmethyl)-1H-1,2,3-triazol-1-yl]pyridine-3-carboxylate, the pyridine ring R1 (C4–C8/N1) and 1H-1,2,3-triazole ring R2 (C9/C10/N2/N3/N4) are planar with r. m. s. deviations of 0.0068 and 0.0006 Å, respectively. The dihedral angle between R1/R2 is 6.58(21)°. The ethyl part of ester group is disordered over two set of sites with occupancy ratio of 0.633(10): 0.367(10). The major part of ester group (C1A/C2A/C3/O1/O2) is roughly planar with r. m. s. deviation of 0.1420 and it is oriented at a dihedral angle of 14.0(5)° with the adjacent pyridine ring. The cyclohexyl ring is in chair form (Cremer-Pople puckering param-

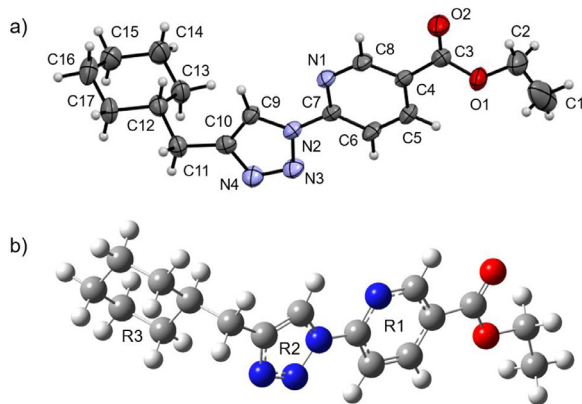


**Fig. 1.** (a) Molecular structure of **1** showing the atoms numbering, with ellipsoids drawn at the 30% probability level; (b) Optimized molecular structure calculated at B3LYP/6-311G(d,p) level of theory.

**Table 2**  
Selected bond lengths (Å), angles and dihedral angles (°) obtained from XRD and DFT methods for compound **1**.

Parameters	Experimental <sup>a</sup>	Calculated <sup>b</sup>
<b>Bond lengths</b>		
O1–C2	1.445(6)	1.450
O1–C3	1.321(5)	1.348
O2–C3	1.192(5)	1.209
N1–C7	1.323(5)	1.330
N1–C8	1.334(4)	1.332
N2–N3	1.360(4)	1.361
N2–C7	1.415(4)	1.413
N2–C9	1.352(4)	1.365
N3–N4	1.314(4)	1.292
N4–C10	1.350(5)	1.375
C9–C10	1.360(5)	1.373
C10–C11	1.493(5)	1.496
<b>Bond angles</b>		
C2–O1–C3	117.7(3)	116.1
O1–C2–C1	114.4(5)	107.5
O1–C3–C4	114.4(3)	112.1
N1–C7–N2	114.7(3)	115.4
N3–N2–C7	120.1(3)	121.3
C10–C11–C12	115.3(3)	115.0
<b>Dihedral angles</b>		
C3–O1–C2–C1	139.0(5)	-179.9
C2–O1–C3–O2	2.2(6)	0.052
C2–O1–C3–C4	-178.4(3)	-179.9
C8–N1–C7–N2	178.8(3)	179.8
N3–N4–C10–C11	-178.9(3)	179.7
N4–C10–C11–C12	-126.9(3)	-84.86

<sup>a</sup> Obtained from X-ray diffraction analysis

<sup>b</sup> Calculated at B3LYP/6-311G(d,p) level of theory.

ters:  $q_2 = 0.016$  Å,  $q_3 = -0.2297$  Å,  $\varphi_2 = 358.16^\circ$ , and  $Q = 0.5171$  Å) with basal plane (C13/C14/C16/C17) [r. m. s. deviation 0.0023 Å] having apical atoms C12 and C15 at a distance of -0.604 (5) Å and 0.625 (6) Å, respectively.

As can be seen from Table 2, the agreement between the experimental and computed geometrical parameters is good. The main average deviation between the computed and experimental bond lengths and bond angles are 0.027 Å and 3.9°, for the O1–C3 bond length and O1–C2–C1 angle, respectively. The N3–N4 bond length of 1.314(4) Å (calculated: 1.292 Å) is slightly shorter than that expected for an N–N single bond (1.42 Å) [33], while the two C–N bond lengths involving the triazole ring are between the characteristic single (1.42 Å) and double bond lengths (1.27 Å) [34]. In contrast, we have observed a longer C–N bond length [N2–C7: 1.415(4) Å] involving the N2 atom of the triazole ring (R2) and the C7 of the pyridine ring (R1). The C3–O1 bond length [1.321(5) Å] shows considerable double-bond character according to the sum of covalent

**Table 3**

Relevant hydrogen bonds geometrical parameters (Å, °) for ethyl 6-(4-(cyclohexylmethyl)-1H-1,2,3-triazol-1-yl)pyridine-3-carboxylate (**1**).

D–H...A	d(D–H)	d(H...A)	d(D...A)	<(D–H...A)
C9–H9...O2 <sup>i</sup>	0.93	2.57	3.457(1)	159
C8–H8...N1 <sup>i</sup>	0.93	2.66	3.426(1)	141
C12–H12...O2 <sup>i</sup>	0.98	2.91	3.858(1)	162
C17–H17A...N4 <sup>ii</sup>	0.97	2.98	3.911(1)	160
C11–H11A...N3 <sup>ii</sup>	0.97	2.76	3.676(1)	158

Symmetry codes: (i)  $-x+1, -y, -z$ ; (ii)  $x+1, +y, +z$ . A= acceptor; D= donor

radii (1.42 Å). In accordance with Table 2 and Fig. 1b, when the X-ray structure of the title compound is compared with its optimized counterparts, slight conformational discrepancies are observed between them. The most significant structural disparities are found in the orientation of the ethyl group, defined by the torsion angle C3–O1–C2–C1 in which the experimental value is found to be 139.0(5)° compared with the computed value (-179.9°). The optimized molecular structure of **1** clearly shows that the ring R3 is in a different orientation compared with the X-ray structure, as can be seen in the N4–C10–C11–C12 dihedral angles [Experimental: -123.9(3)°, calculated: -84.86°]. The differences between observed and calculated geometrical parameters of the title compound can be attributed to the fact that theoretical calculations have been performed with isolated molecules in gas-phase whereas the experimental values correspond to the crystalline state, in which the intermolecular interactions involving the ethyl group play an important role (see below).

In the crystal packing of **1**, molecules are linked through C9–H9...O2 and C8–H8...N1 hydrogen bonds, creating  $R_2^2(18)$  and  $R_2^2(6)$  graph-set motifs, respectively (Fig. 2a, Table 3). The crystal structure of **1** is further stabilized by C–H...N hydrogen bonds, as shown in Fig. 2. The H11A and H17A atoms interact with N3 and N4 atoms of the triazole ring forming C11–H11A...N3 and C17–H17A...N4 hydrogen bonds (Fig. 2d, Table 3). In addition, the overall 3D association is mainly guided by two additional C5–H5...N3 and C1–H1C...N4 hydrogen bonds (Fig. 2e), which exhibit medium directionality and H...N distances longer than the sum of vdW radii.

Apart from hydrogen bonds in the formation of 3D architectures, the X-ray data reveal that the crystal packing also exhibits  $\pi$ ... $\pi$  stacking interactions (Fig. 2b, Table 4), involving the centroids Cg1 (N2–N4/C9/C19) and Cg2 (C4–C8/N1). The geometric parameters reported in Table 4 clearly indicate the presence of weak off-set stacked interactions, as reflected by the inter-centroid Cg1...Cg2 distance of 3.6091(12) Å [35].

In **1**, the centroid of the 6-membered ring (Cg2) of the asymmetric unit is in contact with the O2 atom from the carbonyl group of a nearby molecule through lone pair... $\pi$  interactions (symmetry code: 2-x, -y, -z), with average O2...Cg2 distance of 3.6447(12) Å (Fig. 2c). The shorter separation O2...C6 = 3.524 Å and the remaining distances separating the O-atom from each atom of the pyridine ring are below and above the sum of vdW radii. Hence, the lp(O)... $\pi$  interactions can be classified as weak in the title compound [36]. As shown in Fig. 2c, this self-assembled dimer is also stabilized by C–H... $\pi$  interactions involving the H2A of the ethyl group of one molecule and the triazole ring (Cg1) of another molecule, with H2A...Cg1 distance of 3.68 Å.

### 3.3. Hirshfeld surface analysis

We have performed Hirshfeld surface analysis in order to get further insight into the packing motifs and the contributions of the main intermolecular contacts, which are responsible of the supramolecular assembly of the title compound. Fig. 3a shows

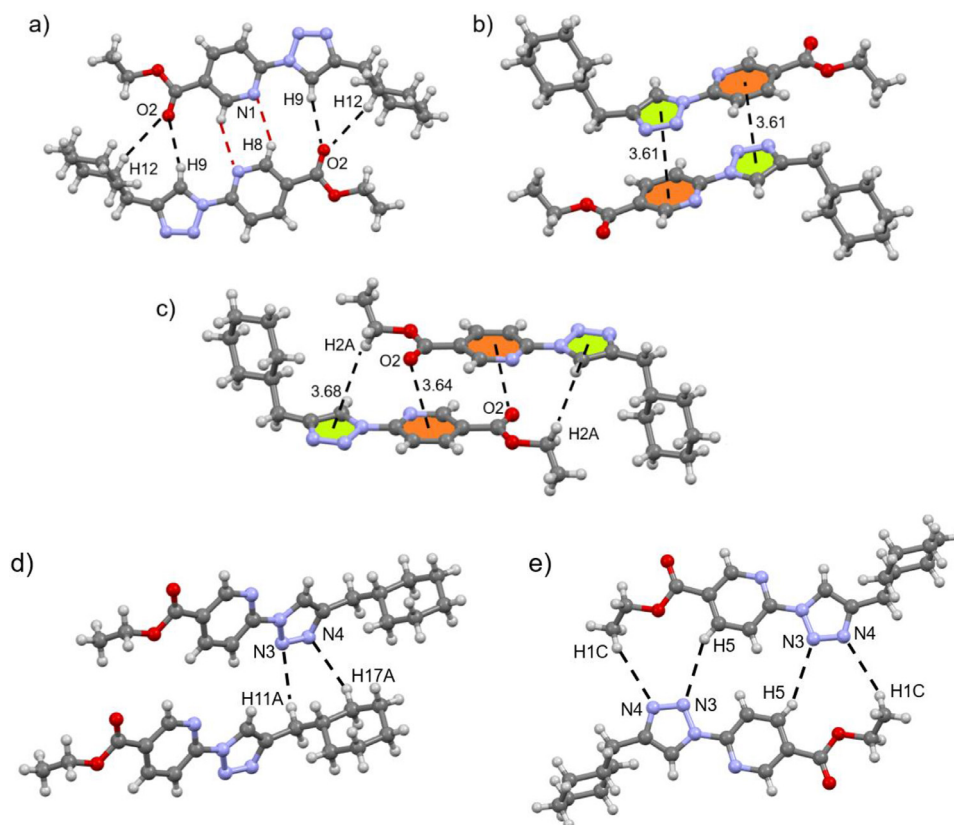


**Fig. 2.** (a) Partial view of the self-assembled dimer formed by C9-H9...O2, C12-H12...O2, and C8-H8...N1 hydrogen bonds; (b) A view of the  $\pi$ ... $\pi$  stacking interactions showing Cg1...Cg2 contacts (Cg1: green, Cg2: orange); (c) Molecular pair stabilized by C2-H2A... $\pi$  and lone pair (O2)... $\pi$  interactions; (d) Partial view of the crystal packing of **1** showing C11-H11A...N3 and C17-H17A...N4 hydrogen bonds; (e) Self-assembled dimer stabilized by C1-H1C...N4 and C5-H5...N3 hydrogen bonds.

**Table 4**

Geometrical parameters ( $\text{\AA}$ ,  $^\circ$ ) for the  $\pi$ -stacking moieties involved in the  $\pi$ ... $\pi$  interactions for ethyl 6-(4-(cyclohexylmethyl)-1H-1,2,3-triazol-1-yl)pyridine-3 carboxylate (**1**)<sup>a</sup>.

Rings I-J	R <sub>c</sub> <sup>b</sup>	R <sub>1v</sub> <sup>c</sup>	R <sub>2v</sub> <sup>d</sup>	$\alpha$	$\beta$	$\gamma$	symmetry
Cg1...Cg2	3.6091(12)	3.4859	3.3578	7.00	21.5	15.0	1-x,1-y,-z
Cg2...Cg2	4.4427(15)	3.5223	3.5223	0.00	37.5	37.5	2-x,-y,-z

<sup>a</sup> Cg1 and Cg2 are the centroids of the N2/N3/N4/C10/C9 and N1/C7/C6/C5/C4/C8 rings, respectively.

<sup>b</sup> Centroid distance between ring I and ring J.

<sup>c</sup> Vertical distance from ring centroid I to ring J.

<sup>d</sup> Vertical distance from ring centroid J to ring I.

Hirshfeld surfaces mapped over  $d_{\text{norm}}$  property, and arrows indicate key contacts with numbers. The corresponding full two-dimensional fingerprint plot and decomposed to show H...N/N...H and H...O/O...H contacts are displayed in Fig. 3b.

The two large adjacent deep-red regions labeled 1 in the  $d_{\text{norm}}$  map represent the H...O/O...H contacts attributed to a pair of C9-H9...O2 hydrogen bonds that forms the inversion dimers. These contacts are visible in the fingerprint plots as a pair of symmetrical spikes at  $(d_e + d_i) \sim 2.4 \text{ \AA}$  (see Fig. 3b) contributing 8.80% to the total Hirshfeld surface area.

The bright regions labeled 2 in the  $d_{\text{norm}}$  represent H...N/N...H contacts associated to C8-H8...N1 hydrogen bonds, which are displayed as a pair of symmetrical sharp spikes at  $(d_e + d_i) \sim 2.5 \text{ \AA}$  in the corresponding fingerprint plot. The proportion of H...N/N...H interactions comprises 14.5% of the total Hirshfeld surface for each molecule in the title compound.

In addition to the above-mentioned hydrogen bonds, the crystal packing of **1** is also stabilized by C-H... $\pi$ , lone pair... $\pi$  and  $\pi$ ... $\pi$  stacking interactions. The evidence of C-H... $\pi$  contacts is clearly visible as the pronounced wings observed on the sides of the fin-

gerprint plots, with  $(d_e + d_i) \sim 3.4 \text{ \AA}$ . The existence of  $\pi$ ... $\pi$  stacking interactions is also justified by the appearance of touching red and blue triangular pairs on the Hirshfeld surfaces mapped over shape index (Fig. 4), and in the flat region delineated by the blue outline above the corresponding aromatic rings on the Hirshfeld surface mapped over curvedness (Fig. 4) [37]. The C...C contacts associated to  $\pi$ ... $\pi$  stacking interactions are visible in the fingerprint plots as a pale green area at around  $d_e = d_i = 1.8 \text{ \AA}$  [38].

The H...H contacts are reflected in the middle of the scattered points in the fingerprint plots, and they have a significant contribution to the total Hirshfeld surfaces in 62.8%.

### 3.4. Energy frameworks analysis

A new feature recently incorporated into *CrystalExplorer17.5* [20] was used for the calculation of pair-wise interaction energies in a crystal by summing up four energy contributions, namely electrostatic ( $E_{\text{ele}}$ ), polarization ( $E_{\text{pol}}$ ), dispersion ( $E_{\text{dis}}$ ) and exchange-repulsion ( $E_{\text{rep}}$ ). The calculations were performed from the monomer wave function at the CE-B3LYP/6-31G(d,p) en-

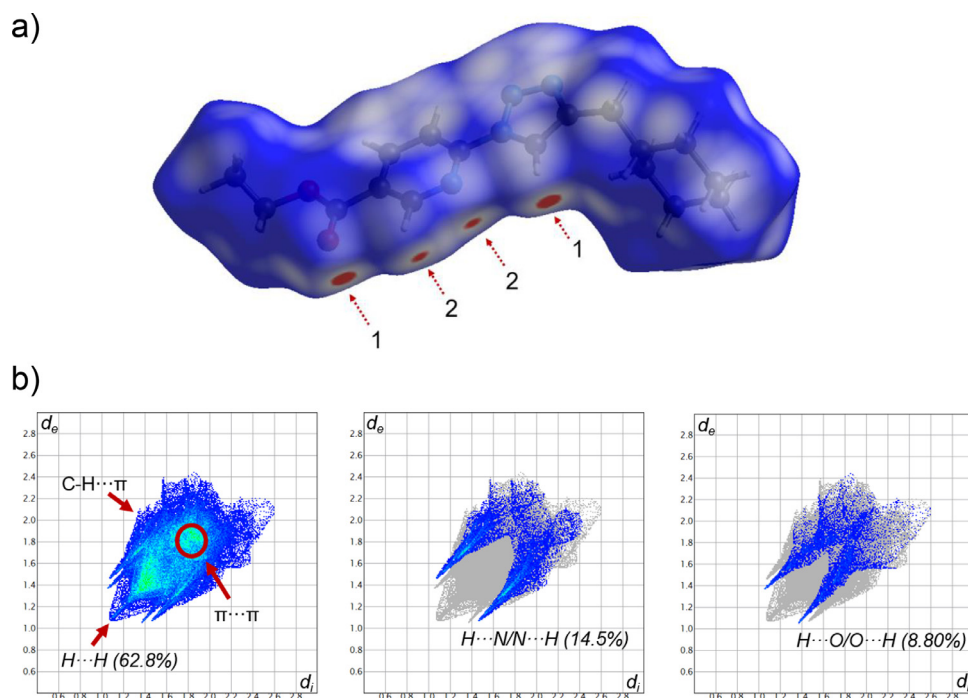
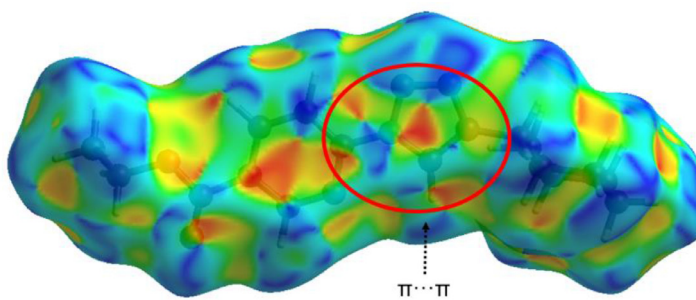


**Fig. 3.** (a) View of the Hirshfeld surface mapped over  $d_{\text{norm}}$  property. Close contacts are labeled as follows: (1) C9-H9...O2 and (2) C8-H8...N1; (b) 2D-fingerprint plots: Full (left) and decomposed into H...N/N...H (center) and H...O/O...H (right) showing percentage of contribution to the total Hirshfeld surface area of the molecule.

### Shape index



### Curvedness

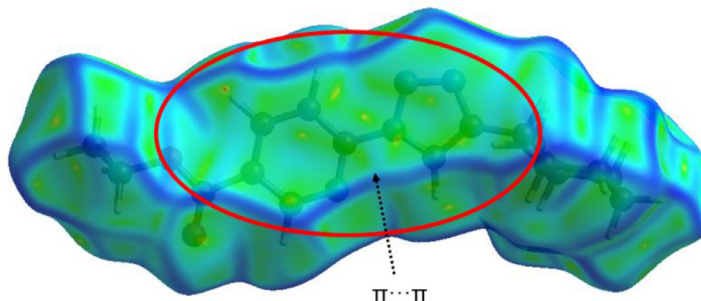


**Fig. 4.** Hirshfeld surfaces of **1** mapped over *shape index* and *curvedness* properties.

ergy model with scale factors to determine total energy  $E_{\text{tot}}$ :  $k_{\text{ele}} = 1.057$ ,  $k_{\text{pol}} = 0.740$ ,  $k_{\text{dis}} = 0.871$ ,  $k_{\text{rep}} = 0.618$ . A cluster of molecules within a radius of 3.8 Å for a central molecule was generated. The results include a color-coded molecular cluster related to the particular interaction energy. Pair-wise energies are represented graphically as framework energy diagrams, which are restricted to electrostatic and dispersion-energy terms, and total energies. The energies are visualized as cylinders linking the centers of mass of the molecules, where the cylinder thickness is proportional to the magnitude of the interaction energy. The cylinders are red for the electrostatic term, green for dispersion term, and blue for total energy.

As illustrated in Fig. 2, the crystal structure of **1** shows five molecular pairs (dimers **1-5**) and the intermolecular interaction energies ( $E_{\text{tot}}$ ) for these dimers along with their partitioned energies are presented in Table 5. As shown in Fig. 2a, dimer **1** is stabilized by three intermolecular interactions (C9-H9...O2, C8-H8...N1 and C12-H12...O2) with an interaction energy of -44.7 kJ/mol (45% contribution of electrostatic energy). The hydrogen bonding geometry (Tables 3 and 5) favours the formation of the C-H...O and C-H...N hydrogen bonds. The second strongest molecular pair (dimer **2**,  $E_{\text{tot}} = -45.0$  kJ/mol) is mainly stabilized by  $\pi$ ... $\pi$  stacking interactions involving the centroids Cg1 and Cg2 (see Fig. 2b). The dispersion energy contributes 91% towards the

**Table 5**

Total interaction energies ( $E_{\text{tot}}$ )<sup>a</sup> partitioned into electrostatic ( $E_{\text{ele}}$ ), polarization ( $E_{\text{pol}}$ ), dispersion ( $E_{\text{dis}}$ ) and exchange-repulsion ( $E_{\text{rep}}$ ) for selected molecular pairs.

Dimer	Symmetry Operation	Involved interactions <sup>b</sup>	d(Å), <(°)	$E_{\text{ele}}$	$E_{\text{pol}}$	$E_{\text{dis}}$	$E_{\text{rep}}$	$E_{\text{tot}}$
<b>1</b>	-x, -y, -z	C9-H9...O2	2.57, 159	-25.8	-5.5	-38.5	32.7	-44.7
		C8-H8...N1	2.66, 141					
		C12-H12...O2	2.91, 162					
<b>2</b>	-x, -y, -z	Cg1...Cg2	3.61	-3.1	-3.4	-64.2	27.0	-45.0
<b>3</b>	-x, -y, -z	C3-O2...Cg2	3.64	-3.0	-2.2	-59.2	25.8	-40.4
		C2-H2A...Cg1	3.68					
<b>4</b>	x, y, z	C17-H17A...N4	2.98, 160	-9.6	-2.8	-43.5	21.6	-36.9
		C11-H11A...N3	2.76, 158					
<b>5</b>	-x, -y, -z	C5-H5...N3	3.05, 151	-13.2	-5.4	-22.4	13.8	-29.0
		C1-H1C...N4	3.12, 155					

<sup>a</sup> Interaction energies in kJ/mol

<sup>b</sup> Cg1 and Cg2 are the centroids of the N2-N4/C19/C9 and N1/C4-C8 rings, respectively.

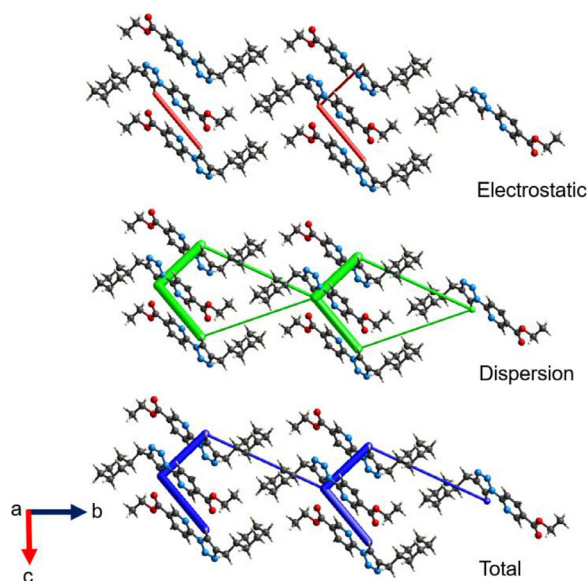


**Fig. 5.** Energy frameworks for the crystal structure of **1** along the *a*-axis, representing the total interaction energy (blue), electrostatic (red) and dispersion (green) components. The energy scale factor is 90 and the energy threshold is 5 kJ/mol.

stabilization of this dimer. Dimer **3** ( $E_{\text{tot}} = -40.4$  kJ/mol) is mainly stabilized lone pair  $\cdots\pi$  interactions between the O-atom of the carbonyl group and the pyridine ring (Centroid Cg2) and supported by intermolecular C-H $\cdots\pi$  (involving H2A and the Cg1 centroid), as shown in Fig. 2c. Two highly directional intermolecular C17-H17A $\cdots$ N4 and C11-H11A $\cdots$ N3 hydrogen bonds generate a molecular dimer **4** ( $E_{\text{tot}} = -36.9$  kJ/mol). This dimer is predominantly dispersive in nature with 78% contribution towards the stabilization. Finally, dimer **5** is stabilized by two weak C-H $\cdots$ N hydrogen bonds, with an interaction energy of -29.0 kJ/mol. We noted that the dispersion energy (55%) is somewhat higher than electrostatic energy (45%) towards the stabilization of this dimer.

We have performed an analysis of the energy frameworks to have a complete picture of all the forces involved in the stabilization of the solid-state geometry of molecules. Fig. 5 shows the energetic results graphically represented in the form of energy frameworks. The partial sum of dispersion energies (-227.8 kJ/mol) is greater than that of electrostatic energies (-54.7 kJ/mol), which evidences that the dispersion energy remarkably dominates over the electrostatic energy in the crystal structure of the title compound. As shown in Fig. 5, the separate energy frameworks for electrostatic (red) and dispersive contribution (green) clearly shows that the cylinders representing the  $\pi\cdots\pi$  stacking interactions has a smaller diameter for electrostatic interaction in comparison to that

**Table 6**

QTAIM parameters [ $\rho(r)$  and  $\nabla^2(\rho)$ ] at the bond critical points (CPs) labelled in Fig. 7.

CP	$\rho(r)$	$\nabla^2(\rho)$
CP1	0.00349	0.01245
CP2	0.00596	0.02458
CP3	0.00709	0.02476

of the dispersive counterpart. This observation graphically signifies that the dispersion interaction dominates over the electrostatic stabilization for the  $\pi\cdots\pi$  contacts.

### 3.5. Theoretical study of intermolecular interactions

The DFT study is devoted to analyze and characterize the hydrogen bonds and  $\pi\cdots\pi$  stacking interactions observed in the solid state.

The molecular electrostatic potential (MEP) of the title compound calculated at B3LYP-D3/def2-TZVP level of theory is shown in Fig. 6. As expected, the most electron rich part corresponds to both N3 and N4 atoms of the triazole ring, with large and negative MEP values (-113 and -142 kJ/mol). Additionally, the MEP value at the O-atom of the carbonyl moiety is also negative (-130 kJ/mol). The MEP values at the H-atom of the triazole and pyridine ring are positive indicating that these atoms could participate in hydrogen bonding interactions with the N and O-atoms. The values over the six- and five-membered rings of the pyridine and triazole moieties are small and opposite in sign, thus favoring the antiparallel stacking.

We have used the QTAIM and NCI plot index analysis (Fig. 7) to further characterize the H-bonded dimer observed in the crystal structure and to evaluate its interaction energy. For the H-bonded dimer (dimer **1**) showed in Fig. 1a, the NCI plot shows intense green isosurfaces between the O and the N-atom of the pyridine ring and the H-atoms of the triazole and pyridine rings corresponding to C-H $\cdots$ O and C-H $\cdots$ N contacts, with a strong dimerization energy ( $\Delta E_1 = -51.49$  kJ/mol). The C-H $\cdots$ O hydrogen bonds are characterized by bond critical points (CP) and bond paths connecting the H and O-atoms (Fig. 7b, Table 6). The computed electron density values are positive and equal to 0.00349 and 0.00596 a.u. for CP1 and CP2, respectively. Similarly, the associated Laplacian of electron density [ $\nabla^2(\rho)$ ] values are positive for both bond CP (see Table 6). All these values fall within the Koch and Popelier limits for hydrogen bonds [39]. Moreover, the QTAIM analyses also evidences the existence of C-H $\cdots$ N hydrogen bonds involving the C8-H8 bond and the N1 atom of the pyridine ring (CP3). In accordance to the results listed in Table 6, the QTAIM parameters for the C8-H8 $\cdots$ N1 hydrogen bond (CP3) are larger than those for C-H $\cdots$ O hydrogen bonds (CP1 and CP2), thus evidencing that the former is

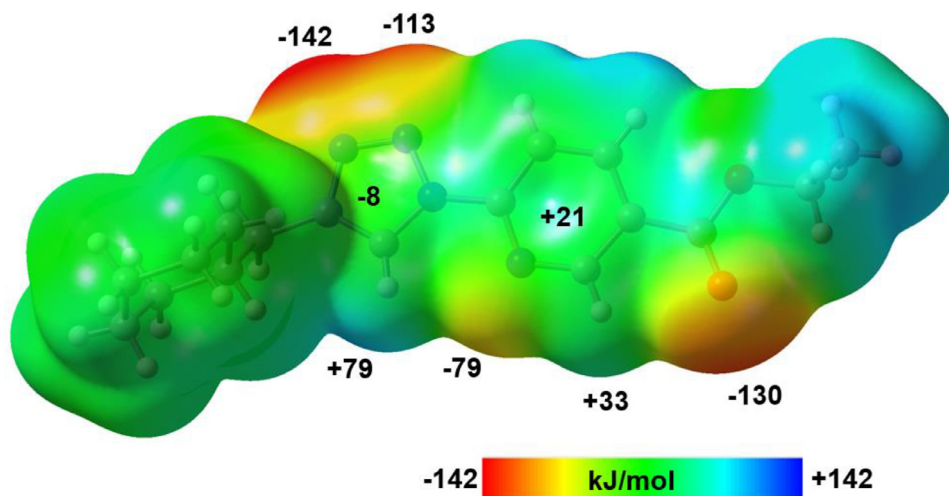


Fig. 6. Molecular electrostatic potential (MEP) surface of **1** at B3LYP-D3/def2-TZVP level of theory (isosurface: 0.001 a.u.). Energies at the selected points in kJ/mol.

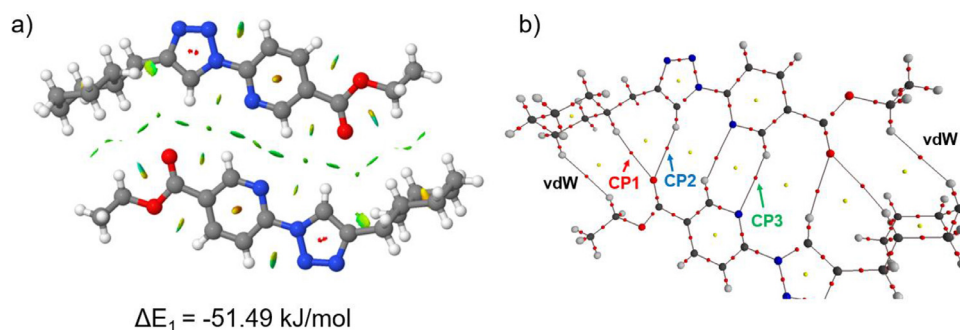


Fig. 7. (a) NCI plot isosurface of the H-bonded dimer of the title compound; (b) Distribution of bonds and ring CPs (red and yellow spheres, respectively).

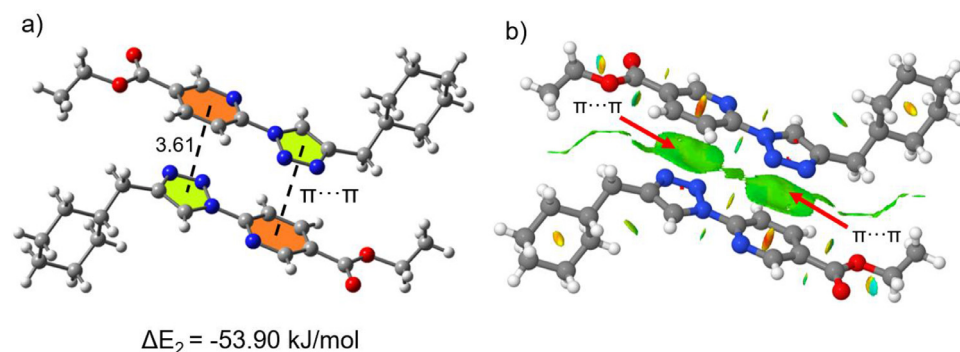


Fig. 8. (a) Self-assembled dimer extracted from the crystal structure; (b) NCI plot isosurface for **1**. Distances in Å.

stronger. As shown in Fig. 7b, the vdW (H...H) interactions play a cooperative role with C-H...O and C-H...N hydrogen bonds in the stabilization of this self-assembled dimer.

Fig. 8a shows the  $\pi$ -stacked dimer (dimer **2**) extracted from the crystal structure of the title compound. The dimerization energy is very large ( $\Delta E_2 = -53.90$  kJ/mol) due to the antiparallel orientation of the dipole. We have also computed the NCI plot in order to characterize the  $\pi \cdots \pi$  stacking interactions observed in dimer **2** (Fig. 8b). It shows two large isosurfaces located between the triazole and pyridine rings thus confirming the existence of two symmetrical  $\pi \cdots \pi$  stacking interactions with a large overlap of the  $\pi$  cloud, in agreement with their short inter-centroid distances (Fig. 8a). The NCI plot also shows several green isosurfaces that are located between the O-CH<sub>2</sub>-CH<sub>3</sub> and the ethylcyclohexane moieties, thus evidencing the existence of additional vdW contacts

apart from the  $\pi$ -stacking interactions upon the formation of the dimer. These vdW interactions also contribute to the enhancement of the  $\pi$ -stacking interactions as a consequence of the H...H contacts, and vice versa.

Fig. 9a shows the self-assembled dimer of **1** (dimer **3**) retrieved from the X-ray structure where the lone pair (O2)... $\pi$  and C-H... $\pi$  interactions are established. The interaction energy of this dimer is also large ( $\Delta E_3 = -51.45$  kJ/mol) due to the combination of lone pair... $\pi$  and C-H... $\pi$  interactions. The NCI plot of dimer **3** is represented in Fig. 9b. The two extended isosurfaces located between the O2 atoms and the pyridine rings are indicative of the existence of the lone pair (O2)... $\pi$  interactions. Additionally, the C-H... $\pi$  interactions are confirmed and characterized by green isosurfaces located between the C-H bond of the methylene group and the  $\pi$ -system corresponding to the pyridine ring.

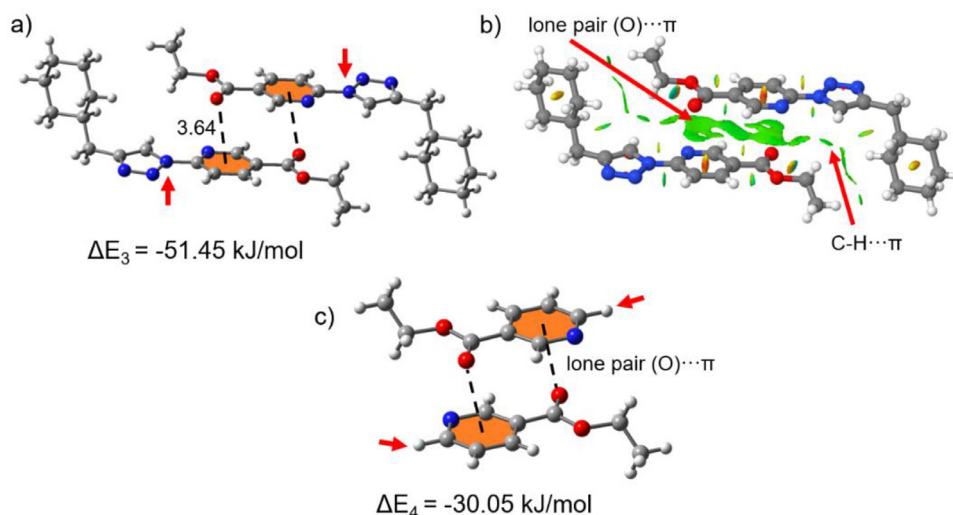


**Fig. 9.** (a) Self-assembled dimer (dimer 3) of **1** extracted from the crystal structure; (b) NCI plot isosurfaces of the dimeric assembly. Distances in Å.

In order to investigate if the contribution of the lone pair $\cdots\pi$  interactions are energetically favorable, we have computed an additional theoretical model, where the N-atom of the triazole ring has been replaced by H-atoms (see small red arrows in Figures 9a and 9c). In this model, the interaction energy is reduced to  $\Delta E_4 = -30.05$  kJ/mol thus suggesting that the lone pair $\cdots\pi$  interactions are attractive.

### 3.6. Vibrational analysis

The experimental and theoretical vibrational wavenumbers of **1** are given in Table S2 (Supplementary material). Comparison between experimental and calculated IR spectra are shown in Figure S1 (Supplementary material). The calculated vibrational wavenumbers are higher than the experimental ones due to neglect of anharmonicity present in the real system (solid state), therefore, these wavenumbers were scaled by using the 0.9668 scale factor for the B3LYP/6-311(d,p) level of theory.

In the region between 4000 and 2000  $\text{cm}^{-1}$  generally appears the C-H stretching modes corresponding to aromatic and aliphatic compounds. In addition, the main vibrational modes of the  $\text{CH}_3$  and  $\text{CH}_2$  are also present in this region. For this compound, the absorption band at 3037  $\text{cm}^{-1}$  is assigned to the antisymmetric  $\text{CH}_3$  stretching mode, whereas the IR bands at 2990 and 2942  $\text{cm}^{-1}$  are attributed to the antisymmetric  $\text{CH}_2$  stretching modes corresponding to the cyclohexane ring (R3). On the other hand, the band at 2916  $\text{cm}^{-1}$  could be assigned to symmetric  $\text{CH}_2$  stretching mode of R3.

The C=O stretching vibration is usually one of the most representative bands observed in the IR spectra of organic compounds, and it generally appears between 1800 and 1600  $\text{cm}^{-1}$  depending on the molecular structure. For the compound under study, the absorption at 1746  $\text{cm}^{-1}$  is assigned to C=O stretching mode (calculated: 1724  $\text{cm}^{-1}$ ). The observed bands between 1614 and 1514  $\text{cm}^{-1}$  are mainly assigned to C-C stretching modes of rings R1 and R2. The C-N stretching mode of the triazole ring (R2) appears as a band located at 1424  $\text{cm}^{-1}$ , in agreement with the calculated value (1421  $\text{cm}^{-1}$ ). The C-O stretching modes with single-bond character generally are predicted between 1400-1000  $\text{cm}^{-1}$ , and for this reason, the IR bands located at 1260 and 1012  $\text{cm}^{-1}$  are assigned to C3-O1 and C2-O1 stretching modes. The bands due to the in-plane C-H bending modes appear between 1595 and 1114  $\text{cm}^{-1}$  (see Table S2).

**Table 7**

LOX IC<sub>50</sub> values of compound **1** and indomethacin used as reference drug.

Compound	LOX IC <sub>50</sub>
<b>1</b>	37.50
Indomethacin (reference drug)	48.25

The IR bands observed between 1000 and 400  $\text{cm}^{-1}$  are assigned to a combination of vibrational modes including C-C, C-O and C-N stretching modes and different in-plane and out-of-plane bending modes, as can be shown in Table S2.

### 3.7. UV-Visible spectra

The UV-Visible spectrum of compound **1** was calculated in ethanol as solvent at B3LYP/6-311G(d,p) approximation. The observed and computed electronic transitions of high oscillator strength are listed in Table S3 (Supplementary material). The comparison between experimental and computed electronic spectra of **1** are shown in Figure S2 (Supplementary material). The TD-DFT calculations predict three intense electronic excitations at 229, 256 and 287 nm which are in agreement with the observed electronic excitations at 222, 259 and 277 nm. The absorption band at 222 nm in the experimental spectrum is assigned to HOMO-7  $\rightarrow$  LUMO, HOMO-1  $\rightarrow$  LUMO+1 and HOMO  $\rightarrow$  LUMO+1 electronic transitions being the second one the most relevant in accordance with the higher percentage of contribution (Table S3). The experimental band at about 259 nm corresponds to HOMO-1  $\rightarrow$  LUMO transition, with 94% of contribution. In addition, the band observed at 277 nm in the experimental spectrum of **1** is attributable to HOMO  $\rightarrow$  LUMO electronic transition, with  $\pi \rightarrow \pi^*$  nature. The most important frontier molecular orbitals (HOMO and LUMO) with their corresponding energies are presented in Figure S3 (Supplementary material). The HOMO involves  $\pi$ -bonding orbitals of the pyridine and triazole rings and the non-bonding character of the carbonyl O-atom. The LUMO exhibits a  $\pi$  anti-bonding character of carbon, nitrogen and oxygen atoms of both triazole and pyridine-3-carboxylate rings.

### 3.8. In-vitro Lipoxygenase Activity

IC<sub>50</sub> values (Table 7) reveal that the synthesized compound has good potential to inhibit lipoxygenase through hydrogen bonds via

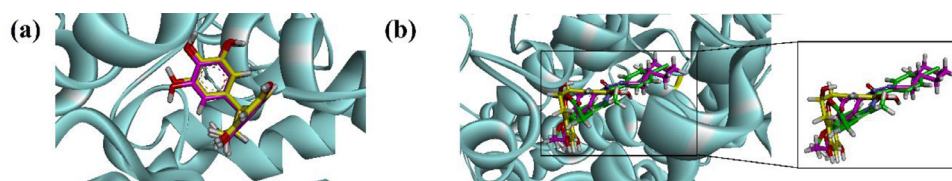


**Fig. 10.** (a) Overlaid orientations of re-docked (pink) and experimental native ligand (EGC) into the binding site of 1JNQ. (b) Three-dimensional overlaid ribbon diagram of native ligand (yellow), indomethacin (green) and compound **1** (pink) into the binding site of lipoxygenase.

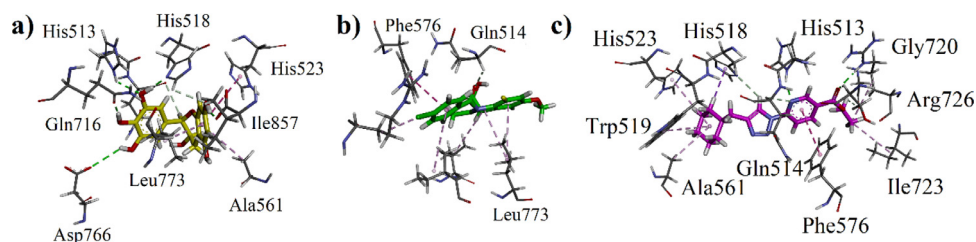
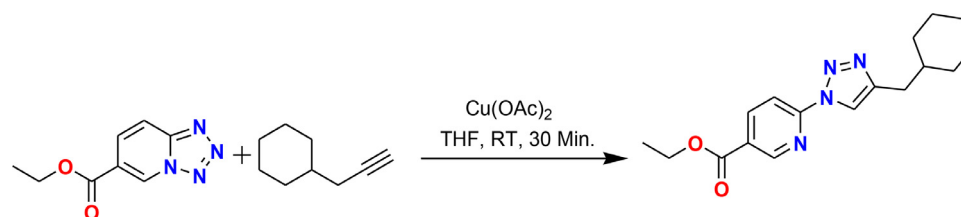


**Fig. 11.** 3D diagrams of the compounds under study (a) native compound; (b) indomethacin and; (c) compound **1**; showing interactions with the amino acid residues (in stick form).



**Scheme 1.** Synthesis of ethyl 6-(4-(cyclohexylmethyl)-1H-1,2,3-triazol-1-yl)pyridine-3-carboxylate (**1**).

nitrogen of pyridine ring as well as carbonyl of ester moiety. Similarly  $\pi \cdots \pi$  stacking interactions of pyridine moiety are also responsible for this phenomena as well. Indomethacin used as a reference drug also shows  $\pi \cdots \pi$  interactions with amino acids. Therefore, both pyridine moieties as well as ester functionality together make this molecule potent toward LOX.

### 3.9. Docking studies

Docking studies were carried out using Molecular Operating Environment (MOE2016.08) software. Crystal structure of lipoxygenase was retrieved from Protein Data Bank (PDB code 1JNQ). Before the docking of the compound, we validated the docking algorithm by re-docking of the native ligand. We performed a complete re-docking protocol to validate the docking algorithm. Native co-crystallized ligand epigallocatechin (EGC) was extracted and prepared in a comparable manner as for others. Started with Triangle matcher algorithm at placement stage and scored by London dG scoring function, rescoring was carried out using ASE and affinity dG scoring functions. Final score was calculated with GBVI/WAS dGScoring function. Best performance in terms of computed RMSD value, conformation, position and pose (orientation) was obtained with Triangle matcher and ASE scoring function. The root mean-square deviation (RMSD) between the re-dock and experimental pose was found 0.97 Å which was found within the threshold limit of < 2.0 Å. The overlaid position and orientation of the re-docked (pink) and experimental native ligand (yellow) into the binding site of 1JNQ is shown in Fig. 10a.

Three-dimensional (3D) binding pose of the synthesized compound overlaid on native ligand and indomethacin is shown in Fig. 10b. 3D interaction diagram of the native ligand, indomethacin and the synthesized compound is shown in Fig. 11a-c. It is shown in Fig. 11a that the native ligand establishes six hydrogen bonding interactions (HBI) with amino acid residues. The

amino acids involved are His518, His513, Gln716, Asp766, Ile857. His523 is involved in  $\pi \cdots \pi$  stacking interactions with the dihydroxy phenyl ring, and Indomethacin forms  $\pi \cdots \pi$  contacts with Phe576 (Fig. 11b). The 3D binding interactions are shown in Fig. 11c. It is revealed from the figure that the compound interacts with the residues through hydrogen bonding interactions. Pyridine ring N-atom is involved in hydrogen bonds with His513. While, carbonyl oxygen forms hydrogen bond with Arg726, Pyridine ring forms  $\pi \cdots \pi$  stacking interactions with Phe576. The binding affinity values of the native ligand, indomethacin, and compound **1** are -9.0532, -6.4650 and -9.5089 kcal/mol, respectively.

## 4. Conclusions

1,4-Disubstituted 1H-1,2,3-triazole derivative was synthesized and fully characterized by spectroscopic as well as single crystal XRD technique. The molecular structure of the title compound was optimized at B3LYP/6-311G(d,p) level of theory showing a very good correlation between the experimental and computed geometrical parameters. The calculated vibrational frequencies for the title compound are consistent with their experimental IR spectrum in the solid state. In addition, we have performed a detailed analysis of the intermolecular interactions present in the crystal structure of **1** by using the Hirshfeld surface analysis and DFT calculations. The crystal packing is mainly governed by C-H $\cdots$ O and C-H $\cdots$ N hydrogen bonds and C-H $\cdots$  $\pi$ , lone pair  $\cdots \pi$  and  $\pi \cdots \pi$  stacking interactions. This study clearly shows that the dispersion energy remarkably dominated over the electrostatic energy in the crystal space, as reflected by the analysis of the energy frameworks. DFT energetic studies with a combination of QTAIM and NCI plots computational tools evidence that the  $\pi \cdots \pi$  and lone pair $\cdots\pi$  interactions observed in the solid state are energetically favorable and attractive.

Docking studies show that the compound forms two hydrogen bonding interactions with the residues. The N-atom of the pyridine ring forms hydrogen bonds with His513, whereas carbonyl O-atom tends to form hydrogen bonds with Arg726. Pyridine ring interacts with Phe576 through  $\pi\cdots\pi$  stacking interactions. In accordance with the results reported in this article, the compound under study may be a good drug candidate in the future.

### Declaration of Competing Interest

The authors declare that they have no known competing financial interests or personal relationships that could have appeared to influence the work reported in this paper.

### CRediT authorship contribution statement

**Muhammad Naeem Ahmed:** Conceptualization, Methodology, Software, Investigation, Writing - original draft, Supervision. **Sadia Shabbir:** Conceptualization, Methodology, Software, Investigation. **Bakhtawar Batool:** Conceptualization, Methodology, Software, Investigation. **Tariq Mahmood:** Conceptualization, Methodology, Software, Investigation. **Umer Rashid:** Conceptualization, Methodology, Software, Investigation. **Muhammad Nawaz Tahir:** Conceptualization, Methodology, Software, Investigation. **M. L. Arias Cassarà:** Conceptualization, Investigation, Writing - original draft. **Diego M. Gil:** Conceptualization, Investigation, Writing - original draft.

### Acknowledgements

MNA is thankful to the University of Azad Jammu and Kashmir for financial support. DMG thanks Agencia Nacional de Promoción Científica y Tecnológica, ANPCyT (PICT 2016-0226) and Secretaría Ciencia, Arte e Innovación Tecnológica, SCAIT-UNT (Project D683) for financial support.

### Supplementary materials

Supplementary material associated with this article can be found, in the online version, at [doi:10.1016/j.molstruc.2021.130283](https://doi.org/10.1016/j.molstruc.2021.130283).

### References

- Z. Xu, S.J. Zhao, Y. Liu, *Eur. J. Med. Chem.* 183 (2019) 111700.
- H. Singh, M. Kumar, K. Nepali, M.K. Gupta, A.K. Saxena, S. Sharma, P.M.S. Bedi, *Eur. J. Med. Chem.* 116 (2016) 102–115.
- K. Kumar, B. Pradines, M. Madamet, R. Amalvict, N. Benoit, V. Kumar, *Eur. J. Med. Chem.* 87 (2014) 801–804.
- R.S. Keri, S.A. Patil, S. Budagumpi, B.M. Nagaraja, *Chem. Biol. Drug. Des.* 86 (2015) 410–423.
- T. Guimarães, M.C.F.R. Pinto, J.S. Lanza, M.N. Melo, R.L. Do Monte-Neto, I.M.M. De Melo, E.B.T. Diogo, V.F. Ferreira, C.A. Camara, W.O. Valenca, R.N. de Oliveira, F. Frezard, E.N. Da Silva Jr, *Eur. J. Med. Chem.* 63 (2013) 523–530.
- D. González-Calderón, M.G. Mejía-Dionicio, M.A. Morales-Reza, A. Ramírez-Villalva, M. Morales-Rodríguez, B. Jauregui-Rodríguez, E. Díaz-Torres, C. González-Romero, A. Fuentes-Benites, *Eur. J. Med. Chem.* 112 (2016) 60–65.
- B. Zhang, *Eur. J. Med. Chem.* 168 (2019) 357–372.
- M. Koteswara Reddy, K.S. Kumar, P. Sreenivas, G.L.D. Krupadanam, K.J. Reddy, *Tetrahedron Lett* 52 (2011) 6537–6540.
- A. Massarotti, S. Aprile, V. Mercuri, E. Del Grosso, G. Grosa, G. Sorba, G.C. Tron, *ChemMedChem* 9 (2014) 2497–2508.
- Q. Zhang, X. Wang, C. Cheng, R. Zhu, N. Liu, Y. Hu, *Org. Biomol. Chem.* 10 (2012) 2847–2854.
- L.N. Andrade, D.P. De Sousa, *Molecules* 18 (2013) 1227–1254.
- (a) K.V. Reddy, T. Hammarberg, O. Rådmark, 2000 *Biochemistry*, 39 1840–1848; (b) M. Ondua, S. Adebayo, L. Shai, S. Lebelo, The anti-inflammatory and anti-nociceptive activities of some medicinal plant species used to treat inflammatory pain conditions in southern Africa, 2016.
- F. Grabarz, C.F. Aguiar, M. Correa-Costa, T.T. Braga, M.I. Hyane, V. Andrade-Oliveira, M.A. Landgraf, N.O.S. Câmara, *Inflammopharmacol* 26 (2018) 491–504.
- F. Farjadmand, H. Arshadi, S. Moghimi, H. Nadri, A. Moradi, M. Eghtedari, F. Jafarpour, M. Mahdavi, A. Shafiee, A. Foroumadi, *J. Chem. Res.* 40 (2016) 188–191.
- (a) M.N. Ahmed, K.A. Yasin, K. Ayub, T. Mahmood, M.N. Tahir, B.A. Khan, M. Hafeez, M. Ahmed, *J. Mol. Struct.* 1106 (2016) 430–439; (b) M.N. Ahmed, K. Ahmad, K.A. Yasin, T. Farooq, B.A. Khan, S.K. Roy, New *J. Chem.* 43 (2019) 11316–11333; (c) M.N. Ahmed, K.A. Yasin, S. Aziz, S.U. Khan, M.N. Tahir, D.M. Gil, A. Frontera, *CrystEngComm* 22 (2020) 3567–3578; (d) M.N. Ahmed, M. Arif, F. Jabeen, H.A. Khan, K.A. Yasin, M.N. Tahir, A. Franconetti, A. Frontera, *New J. Chem.* 43 (2019) 8122–8131.
- (a) M.N. Ahmed, K.A. Yasin, T. Mahmood, F. Wasim, M.H. Khan, M.N. Tahir, S. Zafar, S. Anjum, *Chin. J. Struct. Chem.* 34 (2015) 1830–1840; (b) M.N. Ahmed, K.A. Yasin, M.N. Tahir, I. Arshad, M. Madni, *Chin. J. Struct. Chem.* 34 (2015) 26–32; (c) B. Wang, M.N. Ahmed, J. Zhang, W. Chen, X. Wang, Y. Hu, *Tetrahedron Lett* 54 (2013) 6097–6100.
- M.N. Ahmed, K.A. Yasin, B.A. Khan, M.M. Naser, I. Arshad, M. Irshad, *Chin. J. Struct. Chem.* 35 (2016) 55–60.
- (a) G. Sheldrick, SADABS, Program for empirical X-ray absorption correction, Bruker-Nonius, Madison, WI, 1990; (b) G.M. Sheldrick, 2015 *Acta Crystallogr.* 71C 3–8; (c) H. Andleeb, I. Khan, A. Bauzá, M.N. Tahir, J. Simpson, S. Hameed, A. Frontera, 2018 *Acta Cryst.* 74C 816–829.
- (a) J.J. McKinnon, M.A. Spackman, A.S. Mitchell, *Acta Crystallogr* 60B (2004) 627–668; (b) J.J. McKinnon, D. Jayatilaka, M.A. Spackman, *Chem. Comm.* (2007) 3814–3816; (c) M.A. Spackman, D. Jayatilaka, *CrystEngComm* 11 (2009) 19–32; (d) M.A. Spackman, *Chem. Rev.* 92 (1992) 1769–1797; (e) M.A. Spackman, *Phys. Scr.* 87 (2013) 048103.
- M.J. Turner, J.J. McKinnon, S.K. Wolf, D.J. Grimwood, P.R. Spackman, D. Jayatilaka, M.A. Spackman, *CrystalExplorer* 17 (2017).
- Gaussian 09, Revision D.01, M. J. Frisch, G. W. Trucks, H. B. Schlegel, G. E. Scuseria, M. A. Robb, J. R. Cheeseman, G. Scalmani, V. Barone, B. Mennucci, G. A. Petersson, H. Nakatsuji, M. Caricato, X. Li, H. P. Hratchian, A. F. Izmaylov, J. Bloino, G. Zheng, J. L. Sonnenberg, M. Hada, M. Ehara, K. Toyota, R. Fukuda, J. Hasegawa, M. Ishida, T. Nakajima, Y. Honda, O. Kitao, H. Nakai, T. Vreven, J. A. Montgomery, Jr., J. E. Peralta, F. Ogliaro, M. Bearpark, J. J. Heyd, E. Brothers, K. N. Kudin, V. N. Staroverov, R. Kobayashi, J. Normand, K. Raghavachari, A. Rendell, J. C. Burant, S. S. Iyengar, J. Tomasi, M. Cossi, N. Rega, J. M. Millam, M. Klene, J. E. Knox, J. B. Cross, V. Bakken, C. Adamo, J. Jaramillo, R. Gomperts, R. E. Stratmann, O. Yazyev, A. J. Austin, R. Cammi, C. Pomelli, J. W. Ochterski, R. L. Martin, K. Morokuma, V. G. Zakrzewski, G. A. Voth, P. Salvador, J. J. Dannenberg, S. Dapprich, A. D. Daniels, Ö. Farkas, J. B. Foresman, J. V. Ortiz, J. Cioslowski, and D. J. Fox, Gaussian, Inc., Wallingford CT, 2009.
- (a) A.D. Becke, *J. Chem. Phys.* 98 (1993) 1372–1377; (b) W. Yang C. Lee, R.G. Parr, *Phys. Rev. B: Condens. Matter. Phys.* 37 (1988) 785–789.
- S.B. Boys, F. Bernardi, *Mol. Phys.* 19 (1970) 553–566.
- S. Grimme, J. Antony, S. Ehrlich, H. Krieg, *J. Chem. Phys.* 132 (2010) 154104.
- R.F.W. Bader, *Atoms in Molecules, A Quantum Theory*, Clarendon, Oxford, 1990.
- F. Biegler-König, J. Schönbohn, D. Bayles, *J. Comput. Chem.* 22 (2001) 545–559.
- J. Contreras-García, E.R. Johnson, S. Keinan, R. Chaudret, J.P. Piquemal, D.N. Beratan, W. Yang, *J. Chem. Theory Comput.* 7 (2011) 625–632.
- U.S. Akula, B. Odhav, *J. Med. Plants Res.* 2 (2008) 207–212.
- S. Sekhar, K. Sampath Kumara, S. Niranjana, H. Prakash, *Int. J. Pharm. Sci.* 5 (2013) 257–262.
- S.T. Tanoli, M. Ramzan, A. Hassan, A. Sadiq, M.S. Jan, F.A. Khan, F. Ullah, H. Ahmad, M. Bibi, T. Mahmood, *Bioorg. Chem.* 83 (2019) 336–347.
- S. Tahir, T. Mahmood, F. Dastgir, I. Haq, A. Waseem, U. Rashid, *Eur. J. Med. Chem.* 166 (2019) 224–231.
- D.S. BIOVIA, Discovery studio visualizer, San Diego, CA, USA, 2017.
- P. Pyykkö, M. Atsumi, *Chem. Eur. J.* 15 (2009) 186–197.
- F. Allen, *Acta Crystallogr* B58 (2002) 380–388.
- C. Janiak, *J. Chem. Soc., Dalton Trans.* (2000) 3885–3896.
- M. Egli, S. Sarkhel, *Acc. Chem. Res.* 40 (2007) 197–205.
- A. Di Santo, G.A. Echeverría, O.E. Piro, H. Pérez, A. Ben Altabef, D.M. Gil, *J. Mol. Struct.* 1134 (2017) 492–503.
- S. Syed, S.N.A. Halim, M.M. Jotani, E.R.T. Tiekink, *Acta Crystallogr* E72 (2016) 76–82.
- U. Koch, P.L.A. Popelier, *J. Phys. Chem.* B99 (1995) 9747–9754.